CHAPTER 4 – PILE-SOIL INTERACTION (PSI) FINITE ELEMENT CODE

4.1 INTRODUCTION

PSI (Pile-Soil Interaction) is a 3-D finite element program for analyzing single shafts and shaft groups under vertical, lateral, torsional, and combined loads. The program was developed as a partial fulfillment of a doctoral degree requirement. The Pile-Soil system is modeled as an assemblage of solid elements. The rebar in reinforcement concrete shafts is modeled as a nonlinear bar element; concrete as an elastic, Mohr-Coulomb, or cap model material; and soils are modeled as elastic, Mohr-Coulomb, Hyperbolic, Modified Cam-Clay, Ramberg-Osgood, or cap model materials. The Pile-Soil interface is modeled by the interface element with Mohr-Coulomb or Hyperbolic models. The shaft shape can be square, circular, or H shape; and the dimensions of shafts may vary as a function of depth. The results of an analysis include deformation, stresses, axial force in nonlinear bar element, p-y curve and t-z curve at any depth along a shaft, and shear and moment distribution along the length of a shaft. The stiffness of the equivalent spring for the Pile-Soil system can be formulated from the results of analysis. After the input of geometrical dimensions, a finite element mesh is automatically generated.

4.2 FINITE ELEMENTS

Finite element types used in PSI include 6-node, 8-node, 15-node, and 20-node solid elements for modeling soil and shaft and 8-node and 16-node for modeling the interface between soil and shaft as shown in Figure 35. There are three stiffness components of an interface element: two are for shear stiffness and one for normal stiffness. For modeling the reinforcement, the nonlinear bar element is used. The program automatically creates the model with 8-node or 20-node elements for a structured mesh and 6-node or 15-node elements for an unstructured mesh.

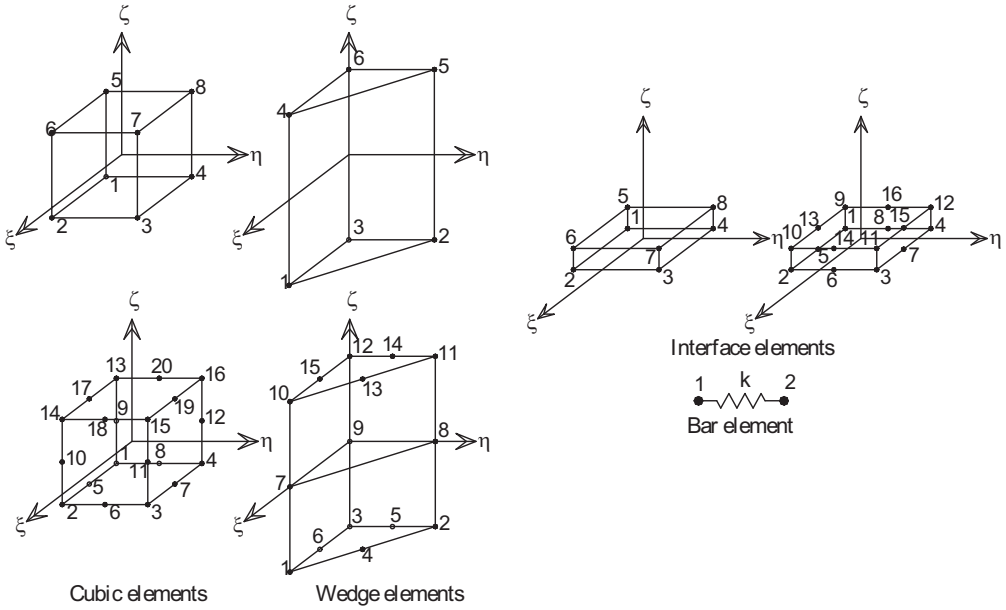

Figure 35. Finite element types.

4.3 ELASTO-PLASTIC RATE INTEGRATION OF DIFFERENTIAL PLASTICITY MODELS

Material characteristic is a critical element of numerical analysis. It can greatly influence the outcome of a numerical prediction. Many constitutive models are available to simulate the soil behavior, and selected ones are presented and implemented in PSI to investigate the model sensitivity. Generally, the associated flow rule is used, unless other wise specified, in the elasto-plasticity ratio to simplify the incremental plasticity computational process and to decrease the CPU time. According to the classical theory of plasticity, the total strain can be decomposed into elastic and plastic parts when stress state reaches yield surface:

$$\begin{aligned} \{d\varepsilon\} &= \{d\varepsilon^e\} + \{d\varepsilon^p\} \\ \{d\varepsilon^e\} &= \{d\varepsilon\} - \{d\varepsilon^p\} \end{aligned} \qquad \text{(Eq. 38)}$$

The Hooke's law relates the stress and elastic strain increments as follows:

$$\begin{aligned} \{d\sigma\} &= \left[E^e\right]\{d\varepsilon^e\} \\ \{d\sigma\} &= \left[E^e\right]\left(\{d\varepsilon\} - \{d\varepsilon^p\}\right) \end{aligned} \qquad \text{(Eq. 39)}$$

In general, the plastic strain increment is written as following the normality rule:

$$\{d\varepsilon^p\} = \lambda \left\{\frac{\partial g}{\partial \sigma}\right\} \qquad \text{(Eq. 40)}$$

where λ is a scalar plastic multiplier that can be calculated by Forward Euler's method or Backward Euler's method (Smith and Griffiths, 1997) and g is the plastic potential function. According to Forward Euler's method:

$$\lambda = \frac{\left[\frac{\partial f}{\partial \sigma}\right]\left[E^e\right]}{\left[\frac{\partial f}{\partial \sigma}\right]\left[E^e\right]\left\{\frac{\partial g}{\partial \sigma}\right\} + h}\{d\varepsilon\} \qquad \text{(Eq. 41)}$$

Substitute Eq. 41 and Eq. 40 to Eq. 39:

$$\{d\sigma\} = \left(\left[E^e\right] - \frac{\left[E^e\right]\left\{\frac{\partial g}{\partial \sigma}\right\}\left[\frac{\partial f}{\partial \sigma}\right]\left[E^e\right]}{\left[\frac{\partial f}{\partial \sigma}\right]\left[E^e\right]\left\{\frac{\partial g}{\partial \sigma}\right\} + h}\right)\{d\varepsilon\} \qquad \text{(Eq. 42)}$$

According to Backward Euler's method:

$$\lambda = \frac{f_{(\sigma)}}{\left[\frac{\partial f}{\partial \sigma}\right]\left[E^e\right]\left\{\frac{\partial g}{\partial \sigma}\right\} + h} \qquad \text{(Eq. 43)}$$

Substitute Eq. 43 and Eq. 40 to Eq. 39:

$$\{d\sigma\} = \left[E^e\right]\{d\varepsilon\} - \frac{f_{(\sigma)}\left[E^e\right]\left\{\frac{\partial g}{\partial \sigma}\right\}}{\left[\frac{\partial f}{\partial \sigma}\right]\left[E^e\right]\left\{\frac{\partial g}{\partial \sigma}\right\} + h} \qquad \text{(Eq. 44)}$$

where f is yield function, g is plastic potential function, and h denotes the hardening parameter that equals to zero for perfectly-plastic materials and constant for an elasto-plastic material with a linear hardening model.

4.4 CONSTITUTIVE MODELS OF SOILS

Six different constitutive models are implemented in PSI, and their use is strictly at the discretion of a user. Two of six models, besides the elastic model, are outlined in the subsequent sections.

4.4.1 Mohr-Coulomb Model

Mohr-Coulomb is the first failure criterion which considered the effects of stresses on the strength of soil. The failure occurs when the state of stresses at any point in the material satisfies the equation below, Chen and Mizuno (1990):

$$|\tau| + \sigma \tan\varphi - c = 0 \qquad \text{(Eq. 45)}$$

where φ and c denote the cohesion and friction angle, respectively. The Mohr-Coulomb criterion can be written in terms of principal stress components (Chen and Mizuno, 1990):

$$\frac{1}{2}(\sigma_1 - \sigma_3) = -\frac{1}{2}(\sigma_1 + \sigma_3)\sin\varphi + c\cos\varphi \qquad \text{(Eq. 46)}$$

The full Mohr-Coulomb (MC) yield criterion takes the form of a hexagonal cone in the principal stress space as shown in Figure 36. The invariant form of this criterion (Smith and Griffiths, 1997) is as follows:

$$f_1 = \frac{I_1}{3}\sin\varphi - \sqrt{\frac{J_2}{3}}\sin\theta\sin\varphi + \sqrt{J_2}\cos\theta - c\cos\varphi \qquad \text{(Eq. 47)}$$

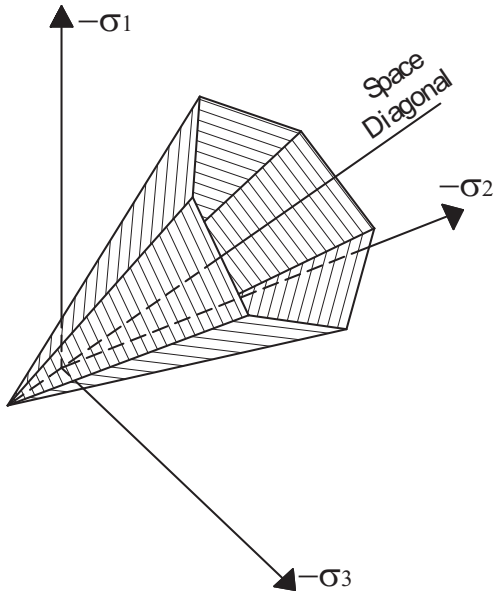

Figure 36. Mohr-Coulomb failure criteria.

In addition to the yield functions, the plastic potential function, the same form as yield function, is defined for the Mohr-Coulomb model by replacing the friction angle, φ, with the dilatancy angle, ψ, in the yield function. The plastic potential function takes the following form:

$$g = \frac{I_1}{3}\sin\psi - \sqrt{\frac{J_2}{3}}\sin\theta\sin\psi + \sqrt{J_2}\cos\theta - c\cos\psi \qquad \text{(Eq. 48)}$$

The dilatancy angle, ψ, is required to model dilative plastic volumetric strain increments as actually observed in dense soils. In reality, soil can sustain no or small tensile stress. This behavior can be specified as tension cut-off. The functions of tension cut-off are:

$$f_2 = \sigma_3 - T\ ;\ f_3 = \sigma_2 - T\ ;\ f_4 = \sigma_1 - T \qquad \text{(Eq. 49)}$$

where T is the maximum tensile stress. For these three yield functions, an associated flow rule is adopted. The MC material parameters include cohesion, c; angle of internal friction, φ; and dilatancy angle, ψ.

4.4.2 Cap Model

The cap model is a plasticity model based on the critical-state concept and the concept of continuum mechanics. The cap model is expressed in terms of the three-dimensional state of stresses and formulated on the basis of the continuum mechanics principle (Desai and Siriwardane, 1984; Chen and Mizuno, 1990).

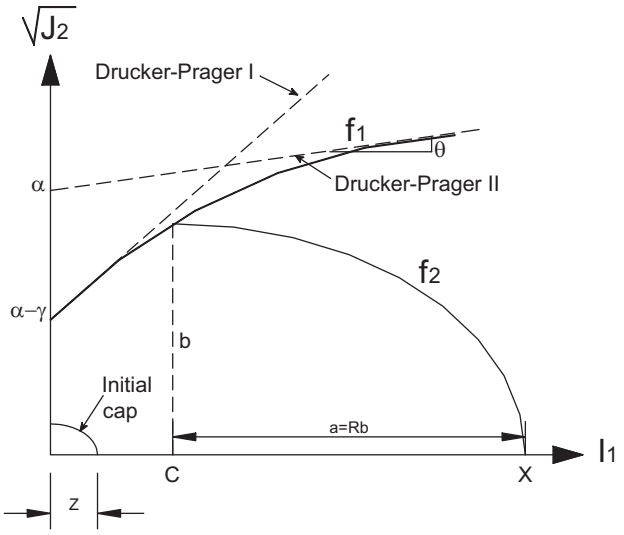

Figure 37. Yield surface for cap model (Desai and Siriwardane, 1984).

The cap model is defined by a dilative failure surface, f_1, and a contractive yield cap surface, f_2. The schematics of the cap model are shown in Figure 37. The expression for f_1 is given by (Desai and Siriwardane, 1984):

$$f_1 = \sqrt{J_2} + \gamma e^{-\beta I_1} - \theta I_1 - \alpha = 0 \qquad \text{(Eq. 50)}$$

where α, β, γ, and θ are material parameters. The quantity $(\alpha - \gamma)$ measures the cohesive strength of the material. These parameters can be determined from triaxial test (Desai and Siriwardane, 1984). During successive yielding, the material undergoes hardening behavior, represented by moving yield surfaces, f_2. An elliptical yield cap for the cohesionless material is given in Eq. 51:

$$f_2 = R^2 J_2 + (I_1 - C)^2 - R^2 b^2 = 0 \qquad \text{(Eq. 51)}$$

where R = the shape factor (the ratio of the major-to-minor axis of the ellipse);
a = $Rb = (X - C)$; X = the value of I_1 at the intersection of the yield cap and the I_1-axis; C = the value of I_1 at the center of the ellipse; b = the value of $\sqrt{J_2}$ when $I_1 = C$; X = a hardening parameter that controls the change in size of the moving yield surface and the magnitude of the plastic deformation; and X = the function of the plastic volumetric strain, ε_v^p, as:

$$X = -\frac{1}{D}\ln\left(1 - \frac{\varepsilon_v^p}{W}\right) + Z \qquad \text{(Eq. 52)}$$

where D, W, and Z are the material parameters, W characterizes the maximum plastic volumetric strain, D the total plastic volumetric strain rate controlling the initial loading moduli, and Z the initiation of plastic volumetric deformation under hydrostatic loading conditions or the pre-consolidation hydrostatic pressure.

4.5 ELASTO-PERFECT PLASTIC MODEL FOR BAR ELEMENT

The bar is elastic with the elastic stiffness, k, when the axial force lies between f_{max} and $f_{min;}$ and it is perfectly plastic at the axial force beyond the above limit, as shown in Figure 38.

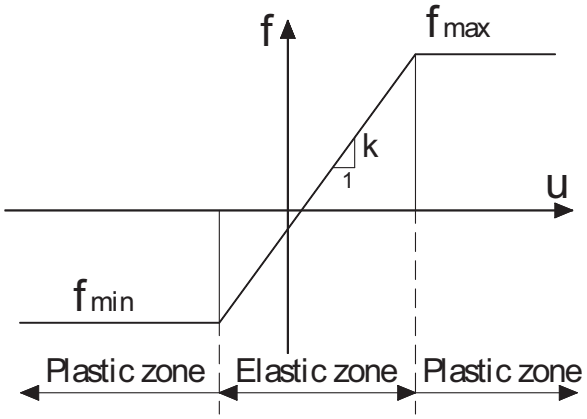

Figure 38. Nonlinear model of bar element.

4.6 CONVERGENCE CRITERIA

PSI performs an iterative solution process for nonlinear analyses. In this procedure, the system stiffness matrix is assembled once and does not change during the iteration. This saves the computation time for the structure with a large number of degrees of freedom. There are two convergence criteria, displacement and balanced load. Both criteria must be met during the computation. If either one is not met whenever the maximum allowable number of iterations is reached, the PSI solver stops running. These criteria can be expressed as:

$$\frac{\delta U^i}{U^i}100\% \le \varepsilon_d \,;\; \frac{\delta R^i}{R^i}100\% \le \varepsilon_d \,;\; \frac{\delta F^i}{F^i}100\% \le \varepsilon_f \,;\text{ and } \frac{\delta M^i}{M^i}100\% \le \varepsilon_f \qquad \text{(Eq. 53)}$$

where U^i, R^i, F^i, and M^i are accumulated transition displacements, rotation displacements, and force and moment at iteration i^{th}, respectively; δU^i, δR^i, δF^i, and δM^i are incremental transition displacements, rotation displacements, and force and moment at iteration i^{th}, respectively; and ε_d and ε_f are user defined tolerances.

4.7 PSI CALIBRATION AND VALIDATION

4.7.1 Case histories for calibration

The accuracy of PSI has been tested by carrying out the analyses of problems or back-analysis of full-scale shaft test by other open or commercial computer codes such as OPENSEES, ABAQUS, PLAXIS, and ANSYS.

Case Study 1: Full-Scale Single Shaft Under Vertical Load

This study has heavily referenced the study on validation and verification of the PLAXIS program (Brinkgreve, 2004). In this document, the full-scale single shaft under vertical load has been analyzed. The same shaft was analyzed by PSI and the results compared to the results using PLAXIS 2D, PLAXIS 3D FOUNDATION, and measured performance.

The shaft with 1.3 m diameter and 9.5 m length is constructed in overconsolidation clay. The parameters of soil profile are shown in Table 6. The loading system includes two hydraulic jacks, one reaction beam, and sixteen anchors supporting the reaction beam. In the PSI analysis, 20-node cubic elements are used. Because of the symmetric condition, only one-fourth of the Pile-Soil system is modeled and analyzed as shown in Figure 39. One-fourth of the soil volume is 25-m by 25-m and 16-m deep. The vertical load at the shaft top is modeled by the equivalent joint loads. The concrete shaft properties used in the linear elastic model are: Young's modulus $E = 3x10^7$ kPa, Poisson's ratio $\nu = 0.2$, and unit weight $\gamma = 24$ kN/m^3. Three coefficients of earth pressure values are considered: 1) $K_0 = 1 - \sin\varphi = 0.62$, 2) $K_0 = \nu/(1-\nu) = 0.43$, and 3) $K_0 = 0.8$ for overconsolidation clay and other soil properties as shown in Table 6.

Table 6. Material parameter for soil data (Brinkgreve, 2004)

Parameter	Value	Unit
Material model	Mohr-Coulomb	-
Type of material behavior	Drained	-
Gravity, γ_s	20	kN/m^3
Young's modulus, E_s	60000	kPa
Poisson's ratio, ν	0.3	-
Cohesion, c	20	kPa
Friction angle, φ	22.7	deg.
Dilatancy angle, ψ	0	deg.

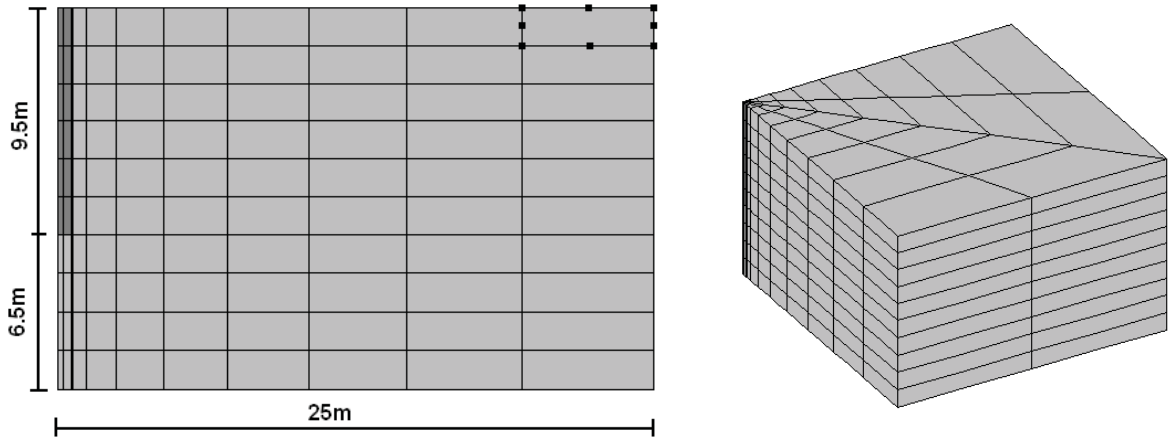

Figure 39. Side view and 3D view of finite element mesh.

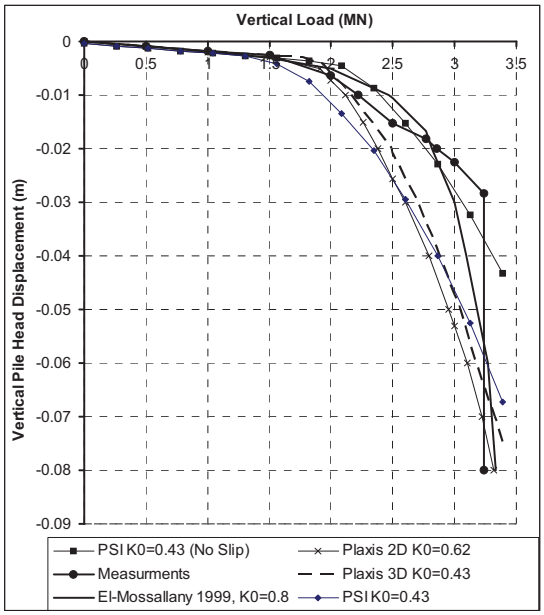

Figure 40. Comparison between PSI, PLAXIS, BEM, and test results.

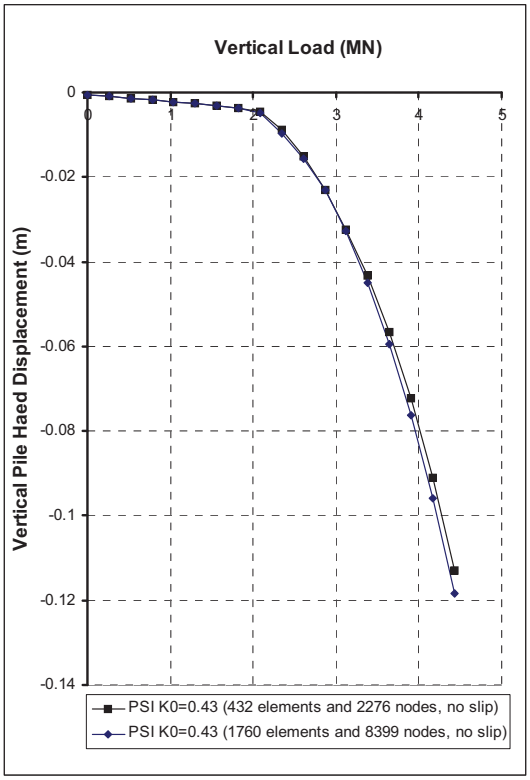

Figure 41. Effect of finite element mesh size on load-displacement curves.

The load-settlement curves are shown in Figure 40. Under a load of 1500 kN, the results of all numerical analyses agree well with test results. At a higher load, however, the results begin to vary depending on the initial stresses and the soil shaft interface. Figure 40 shows that the PSI analysis is close to the PLAXIS 3D analysis but stiffer than the PLAXIS 2D at the same initial condition ($K_0 = 0.43$) with the soil shaft interface. The PSI analysis with no soil shaft interface slip permitted gives the best agreement with the test results.

To assess the mesh density effect, two finite element mesh cases with a different number of elements and nodes were used, and the difference was not significant as shown in Figure 41.

Case Study 2: Colorado DOT Drilled shafts for Noise and Sound Barriers

The lateral load test on a drilled shaft (Shaft #1) used to support noise and walls was performed, Report No. CDOT-DTD-R-2004-8. The diameter of the tested shaft was 0.762 m (2.5 ft); length was 4.096 m (20 ft); and the distance from the shaft top to the ground surface was 1.42 m (437 ft). Two simulations were performed using (1) the soil properties from the triaxial test results and (2) the soil properties adjusted for achieving the best match between the FEM predictions and the test data. The commercially available finite element code, ABAQUS, was used to simulate the lateral shaft load test in CDOT's research.

The same material parameters were used in the PSI analyses. No attempt using PSI was made to achieve the best match. Both programs use the Mohr-Coulomb soil model with some differences: in ABAQUS, the hardening rule is considered in which cohesion depends on the plastic strain; in PSI, cohesion is defined at the zero plastic strain. The soil properties are shown in Table 7 and Table 8. The elastic Young's modulus of shaft is selected as $34.5x10^6$ kPa (5000 ksi), and Poisson's ratio is 0.2.

Figure 42 shows the PSI finite element mesh for only one-half of the soil shaft system for symmetry. The upper part and around the shaft surface of the model is meshed finer than the lower part to get better results for the lateral load analysis.

Table 7. Soil parameters from triaxial test results.

Layers (m)	Young's modulus (kPa)	Cohesion (kPa)
0-0.762	28579.7	71.45
0.762-1.370	22919.0	53.85
1.370-1.980	22919.0	53.85
1.980-3.050	11142.0	47.63
3.050-3.810	54444.0	253.00
3.810-4.580	23982.0	253.00

Table 8. Adjusted soil parameters for match case.

Layers (m)	Young's modulus (kPa)	Cohesion (kPa)
0-0.762	149691.40	62.13
0.762-1.370	149691.40	48.32
1.370-1.980	149691.40	48.32
1.980-3.050	149691.40	48.32
3.050-3.810	47405.04	342.00
3.810-4.580	47405.04	41.40

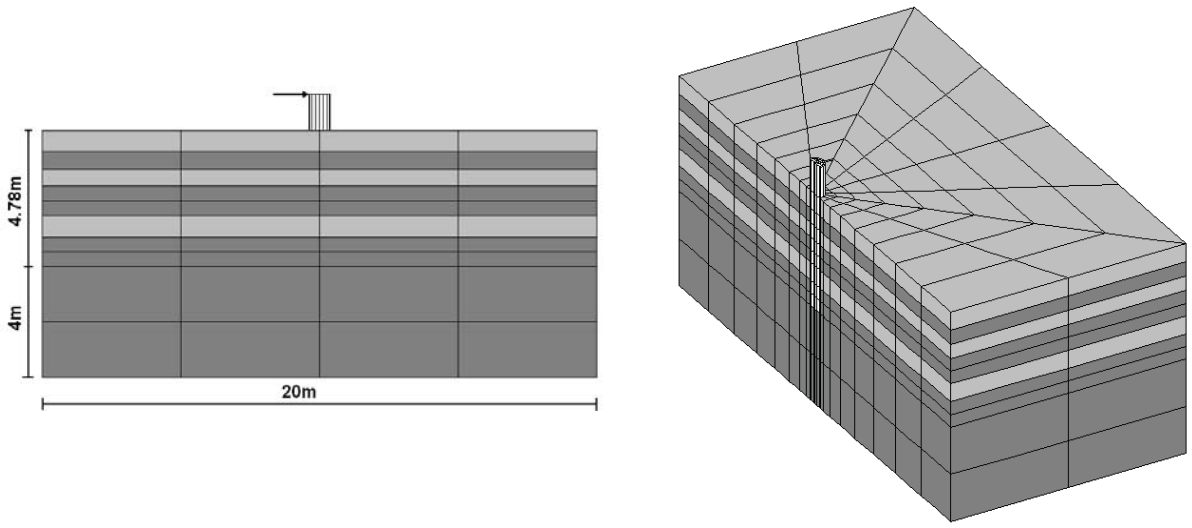

Figure 42. Side view and 3D view of finite element mesh.

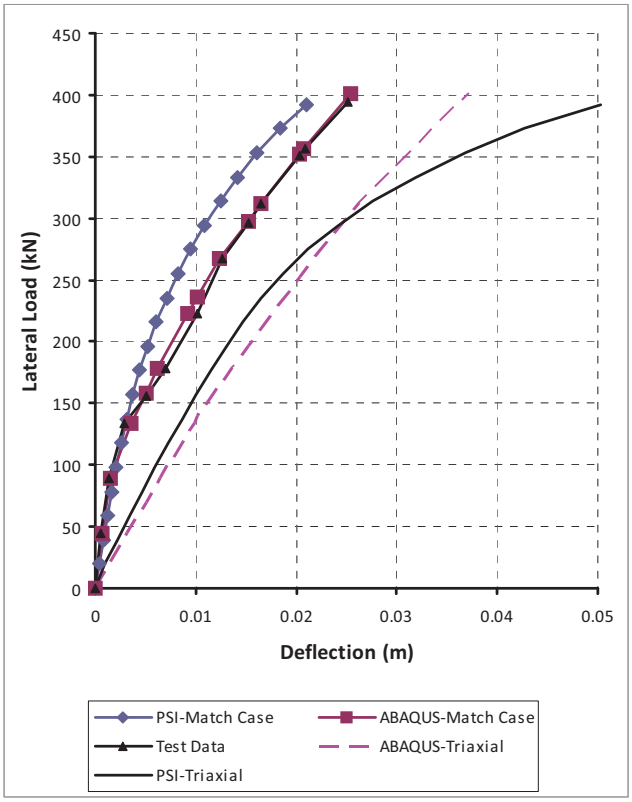

Figure 43. Comparison of the result between PSI, ABAQUS, and test data.

When the triaxial test results were used, both the ABAQUS and PSI analyses showed softer behavior. When the best matched parameters for the ABAQUS were used, the PSI analysis shows a slightly stiffer behavior. In general, the PSI results agreed well with the ABAQUS results as shown in Figure 43.

Case Study 3: Socketed Shaft in Homogeneous Soil

The model of socketed shaft in homogeneous soil shown in Figure 44 was used in the verification of the 3-D ANSYS finite element code (Brown, et al., 2001). In the ANSYS analysis, the shaft and soil were modeled using 8-node cubic elements; a 3-D point-to-surface contact element was used to model the Pile-Soil interface. In the PSI analysis, soil and shaft are modeled by 20-node cubic elements. Soil properties are shown in Table 9. The shaft configuration in Figure 44 is used in the ANSYS and PSI analyses. The behavior of shaft is assumed elastic, with Young's modulus $E = 2x10^7$ kPa and Poisson's ratio $\nu = 0.3$. The soil model in the PSI analysis is the Mohr-Coulomb or the cap model with no cap effect similar to the Drucker-Prager model in the ANSYS analysis. Only the failure envelope parameter, α, and the failure envelope linear coefficient, θ, are considered in the cap model. The lateral load and displacement curves are shown in Figure 45. The PSI analyses using the Mohr-Coulomb and the cap models and the ANSYS using the Drucker-Prager model give nearly identical results.

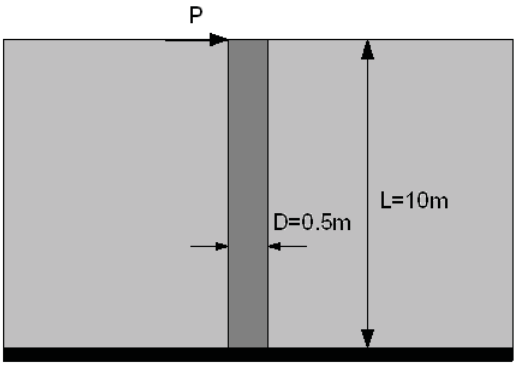

Figure 44. Socketed shaft (Brown, et al., 2001).

Table 9. Material parameter for soil data (Brown, et al., 2001).

Parameter	Value	Unit
Material model	Mohr-Coulomb, cap	-
Type of material behavior	Drained	-
Soil submerged unit weight, γ_s	11.8	kN/m^3
Young's modulus, E_s	20000	kPa
Poisson's ratio, ν	0.45	-
Cohesion, c (For the Mohr-Coulomb model)	34	kPa
Friction angle, φ (For the Mohr-Coulomb model)	142	deg.
Dilatancy angle, ψ (For the Mohr-Coulomb model)	142	deg.
Failure envelope parameter, α (For the cap model)	41.6	kPa
Failure envelope linear coefficient, θ (For the cap model)	0.1207	-

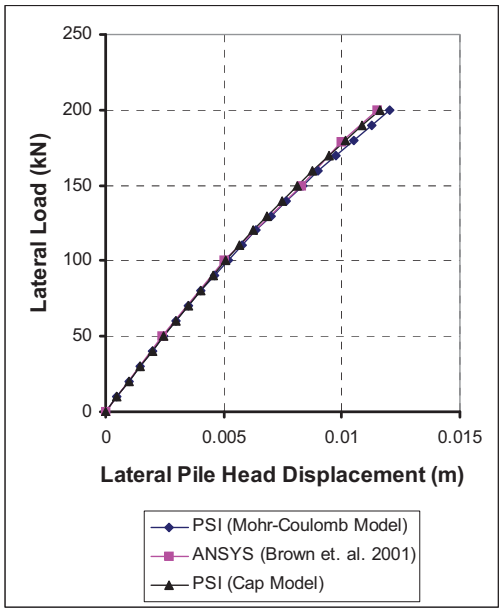

Figure 45. Comparison of shaft head displacement for single socketed shaft.

Case Study 4: Single Shaft under Vertical Load

The PSI analysis was carried out on the single shaft under vertical load. The shaft was installed and tested near the University of California, Berkeley, campus. The analysis was performed by Wang and Sita (2004) using OPENSEES. The 0.762-m (2.5-feet) diameter circular cast-in-place shaft was embedded to a depth of 5.79 m (19 feet). The soil was hard to stiff sandy clay, medium dense sandy silt, and dense clayey sand. Above the depth of about 2.2 m, soil was overconsolidation. Below 4-m deep, the undrained shear strength varied linearly with depth; and the estimated coefficient of earth pressure at rest K_0, was 0.5. The undrained shear strength and the coefficient of earth pressure at rest vary from the 2.2-m deep to the ground surface as shown in Figure 46. For the homogeneous soil profile analysis, the undrained shear strength was the averaged undrained shear strength over the shaft length plus one shaft diameter and the coefficient of earth pressure at rest K_0 assigned to be equal to 0.5. Homogeneous soil properties were: Young's modulus 10^5 kPa, Poisson's ratio 0.49, total unit weight 19.62 kN/m^3, and undrained shear strength 84 kPa. The shaft was modeled elastic with Young's modulus $E = 20x10^6$ kPa and Poisson's ratio $\nu = 0.1$.

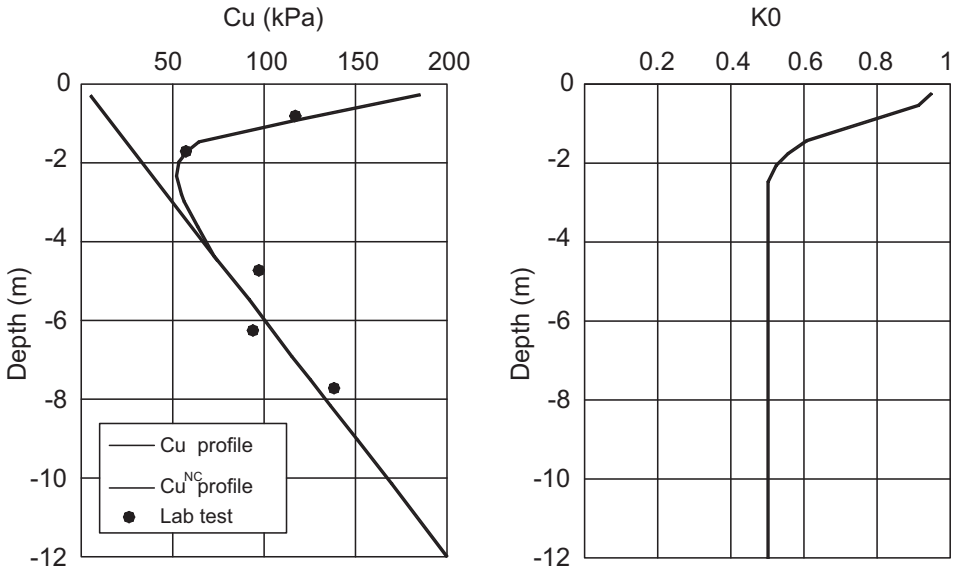

Figure 46. C_u and K_0 profiles (Wang and Sita, 2004).

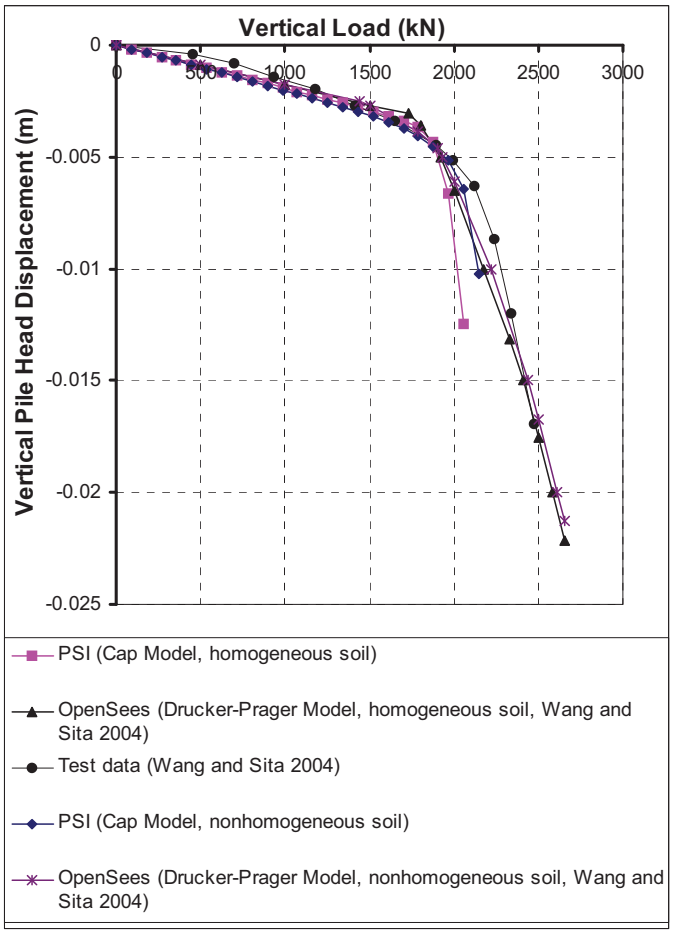

Figure 47. Comparison of the result between PSI, OPENSEES, and test data.

As shown in Figure 47, all analysis results using PSI and OPENSEES show an excellent agreement with the measured performance of the single shaft under a vertical load.

Summary and conclusions

A nonlinear finite element analysis computer code, named **PSI** (**Pile-Soil I**nteraction), was developed in the Center for Geotechnical Engineering Science (CGES) at the University of Colorado at Denver and Health Sciences Center for the analysis of single shafts and shaft groups under all load types singularly or combined, static or dynamic. Six different soil models and two different concrete models are implemented for the convenience of users. The PSI code was developed with the user friendly concept in mind. To assess the validity of PSI, the single shaft performances under vertical or lateral load from four different case studies were analyzed using PSI. The PSI results were compared to the measured load test results and analysis of the results using PLAXIS 2D, PLAXIS 3D, ANSYS, and ABAQUS.

- Good agreements were achieved between the PSI results and the measured shaft-load test results under vertical or lateral load conducted at the Colorado DOT (Jamal Nusairat, et al., 2004); Brinkgreve (2004); and UC Berkeley (Wang, et al., 2004).
- Good agreements were also achieved between the PSI results and the analysis results using PLAXIS 2D, PLAXIS 3D, ABAQUS, and ANASYS by the authors cited in the article.
- The above agreement indicates that the **PSI code** is effective in assessment of single shaft performance under vertical and/or lateral loads.

The subsequent development tasks will include: the comparison with further measurements and LSHAFT results, the analysis of shafts under different loads singularly or combined, the static and dynamic analyses of single or shaft groups, and assessment of group efficiency. CGES is also embarking on the development of the nonlinear SSI Finite Element Analysis Code (**S**oil-**S**tructure **I**nteraction) for the analysis of soil-structure interaction analysis of high-rise buildings under static and dynamic loads.

4.7.2 Comparative study between PSI and LS-DYNA codes

The finite element code PSI was used exclusively in the research on the effect of anomalies on drilled shaft capacities. To ensure that results produced by PSI are reasonable, selected cases were analyzed by both the PSI and the LS-DYNA codes. The latter code was initially developed at the Lawrence Livermore National Laboratory. Its commercial version has been available for many years. Numerical static shaft-load tests were performed in this comparative study. The dimensions of the finite element model are shown in Figure 48. It is assumed that the shaft-load test exhibits an axisymmetric condition, hence only a quarter of the model about the central axis was analyzed. Boundary conditions of the model are also shown in Figure 48. In order to reduce the discrepancy in the analytical results, the finite element mesh (see Figure 49) for the load test model was kept identical in both PSI and LS-DYNA. In addition to the finite element mesh, material parameters for the concrete shaft and soil were also kept the same. Throughout the entire comparative study, the concrete shaft was simulated by the cap material model. For different cases, soil was simulated either by the elastic model or the cap material model. Table 9 summarizes the material parameters used in the comparative study.

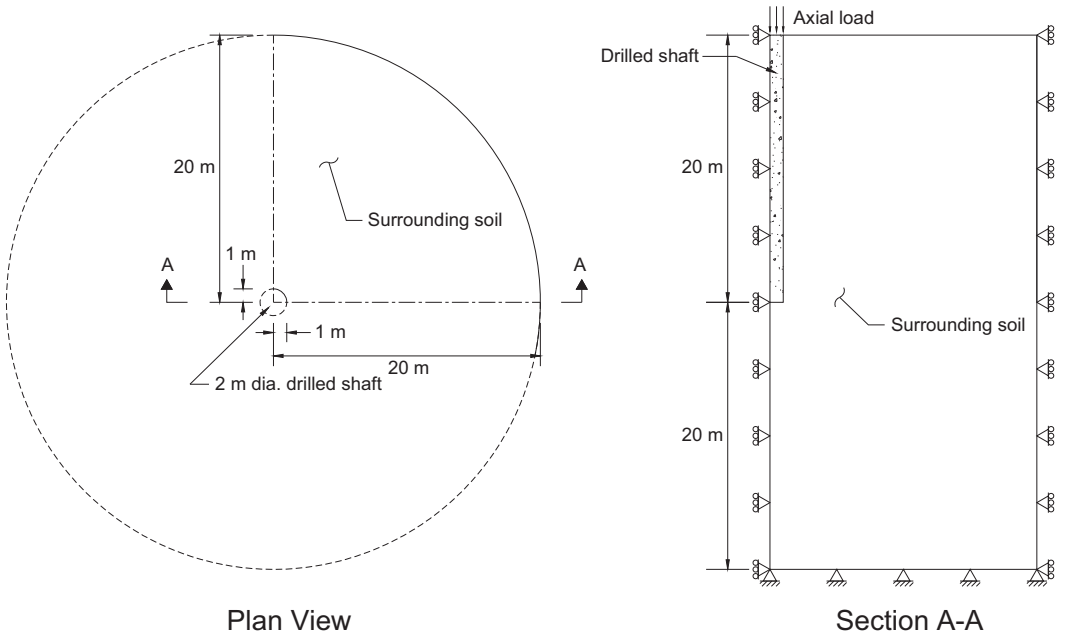

Figure 48. Schematics of numerical shaft-load test.

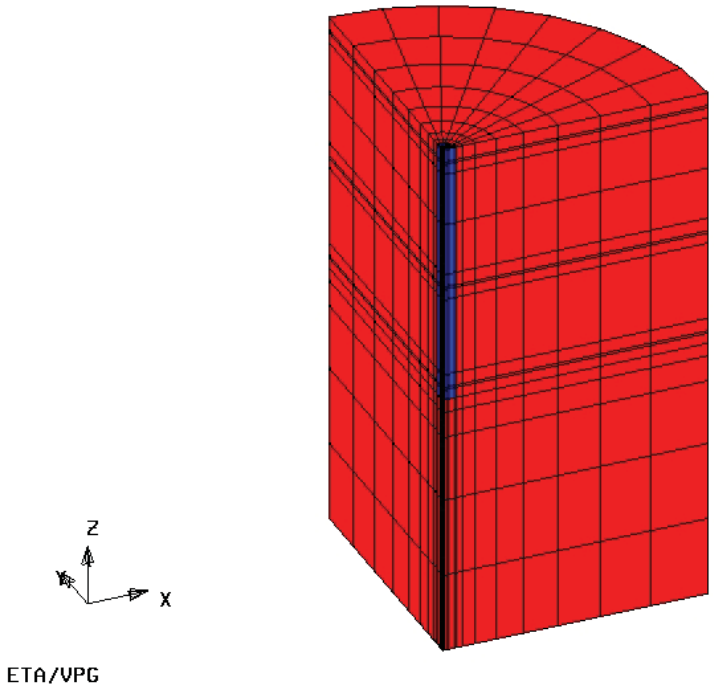

Figure 49. Finite element mesh for the numerical shaft-load test (axisymmetric condition).

Table 10. Material parameters used in the comparative study.

Material	Concrete	Soil	
Parameter	Cap model	Elastic model	Cap model
Density, ρ (kg/m^3)	2250	1719	1719
Bulk modulus, K (MPa)	11961.8	209	209
Shear modulus, G (MPa)	8971.3	40.4	40.4
Failure envelope parameter, α (kPa)	10021	-	0
Failure envelope linear coefficient, θ	0.0928	-	0.2815
Failure envelope exponential coefficient, γ (kPa)	0	-	0
Failure envelope exponent, β (kPa)$^{-1}$	2.35E-07	-	0
Cap surface axis ratio, R	2.3	-	1.6
Hardening law exponent, D (kPa)$^{-1}$	1.77E-07	-	4.00E-04
Hardening law coefficient, W	0.1	-	0.00791
Hardening law exponent, X_o (kPa)	0	-	Varies

The concrete material is assumed to have a compressive strength (f'_c) of 20.7 MPa (3000 lb/in^2). The modulus of elasticity of concrete (E) was determined to be 21,531 MPa using $E = 4732.4\sqrt{f'_c}$ MPa with f'_c = 20.7 MPa ($E = 57{,}000\sqrt{f'_c}$ psi with f'_c = 3000 lb/in^2). The bulk modulus (K) and shear modulus (G) for concrete shown in Table 10 were determined using E = 21,531 MPa and an assumed Poisson's ratio $\nu = 0.2$. The stress strain curve under numerical unconfined compression test is shown in Figure 50. As for the soil, it was assumed to be a dense sand with friction angle $\varphi' = 36°$. Numerical triaxial compression tests under different confining pressures were performed, and the stress strain curves are shown in Figure 51. Note that the hardening law exponent X_o varies in Table 10. X_o is assumed to be related to the overburden pressure (σ_v) and lateral earth pressure (σ_h) with $X_o = \sigma_v + 2\,\sigma_h$ and $\sigma_h = (1 - \sin\varphi')\,\sigma_v$.

The first case considered examines the effect of soil models (i.e., elastic model versus cap material model). Numerical static shaft-load tests were performed with no anomalies in the shaft and with no contact interface between the shaft and the surrounding soil. The load-settlement curves from both finite element codes are presented in Figure 52. Nearly identical results are observed with the elastic soil model. Good agreement is also observed with soil simulated by the cap material model. Note that LS-DYNA produces slightly higher stiffness before yielding than the PSI in the first case. The second case examines the effect of anomaly near the top of the shaft, Figure 53, with no contact interface. The results of the second case are shown in Figure 54, where good agreement is observed. A similar trend is noted between the cases with soil modeled by the cap material model; LS-DYNA produces slightly higher stiffness when the applied load is low and shows a softer response when the load is high.

The third case examines the effect of contact interface between the shaft and soil. The input required for the contact interface for both PSI and LS-DYNA is the Coulomb friction coefficient. The friction coefficient is assumed to be equal to the value of tan φ' (tan 36° = 0.73). In PSI, two additional parameters are needed in defining the contact interface, which are the normal and

shear stiffness of the contact interface. Both the normal and shear stiffness are related to the elastic properties (i.e., modulus of elasticity E and Poisson's ratio ν) of the soil. The analytical results for perfect shaft with contact interface are shown in Figure 55, where good agreement between the two codes is again observed. Consistent with the prior two cases, LS-DYNA generates higher stiffness before yielding than PSI. With the introduction of contact interface, PSI shows a distinct yield point and a soft response post-yielding (more so than LS-DYNA). Note that both PSI and LS-DYNA suggested that introduction of contact interface numerically lowers the load carrying capacity of shafts (see Figures 52 and 55).

It is concluded from this comparative study that the PSI and LS-DYNA analysis results are in good agreement in shaft capacity computation. The minor discrepancy is attributed to the constitutive modeling of soil, element formulation, and treatment of the contact interface. This comparison attests to the validity of the PSI computer code in the analysis of the shaft capacity. With more constitutive models implemented, the PSI code is considered more versatile and will be adopted in this study. In the study proposal, the GAP code developed by Summit Peak, Inc., was selected for the verification of the effectiveness of the PSI code. However, the negotiation for the right to use the GAP code was not successful; and the idea was dropped from further consideration.

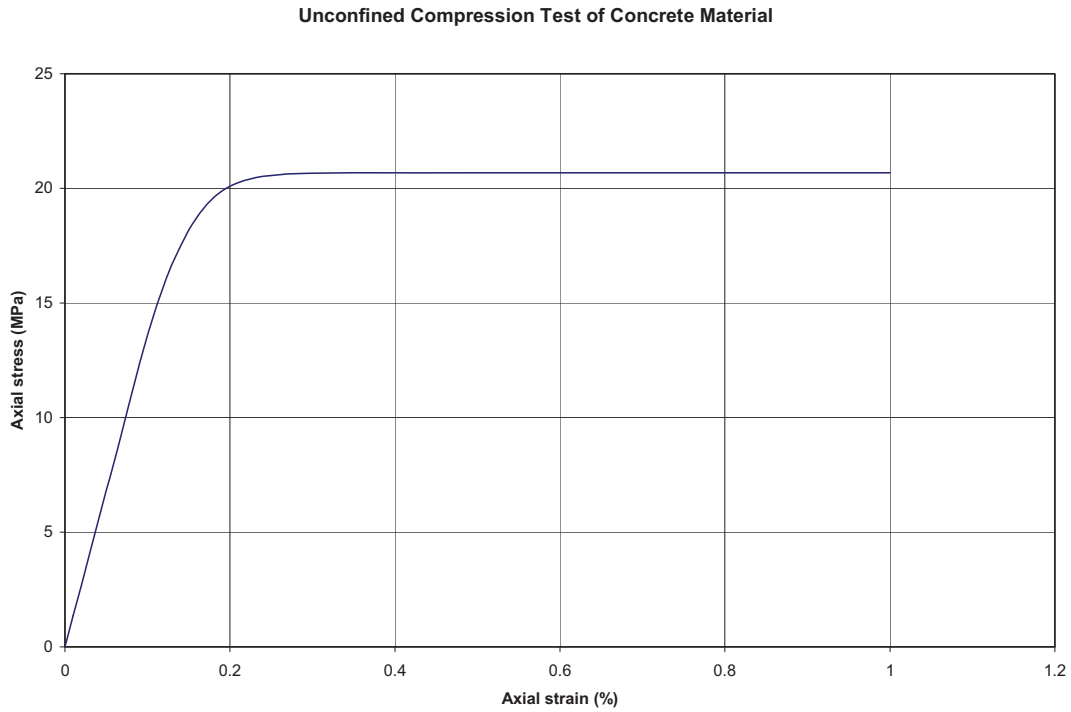

Figure 50. Numerical unconfined compression test for concrete.

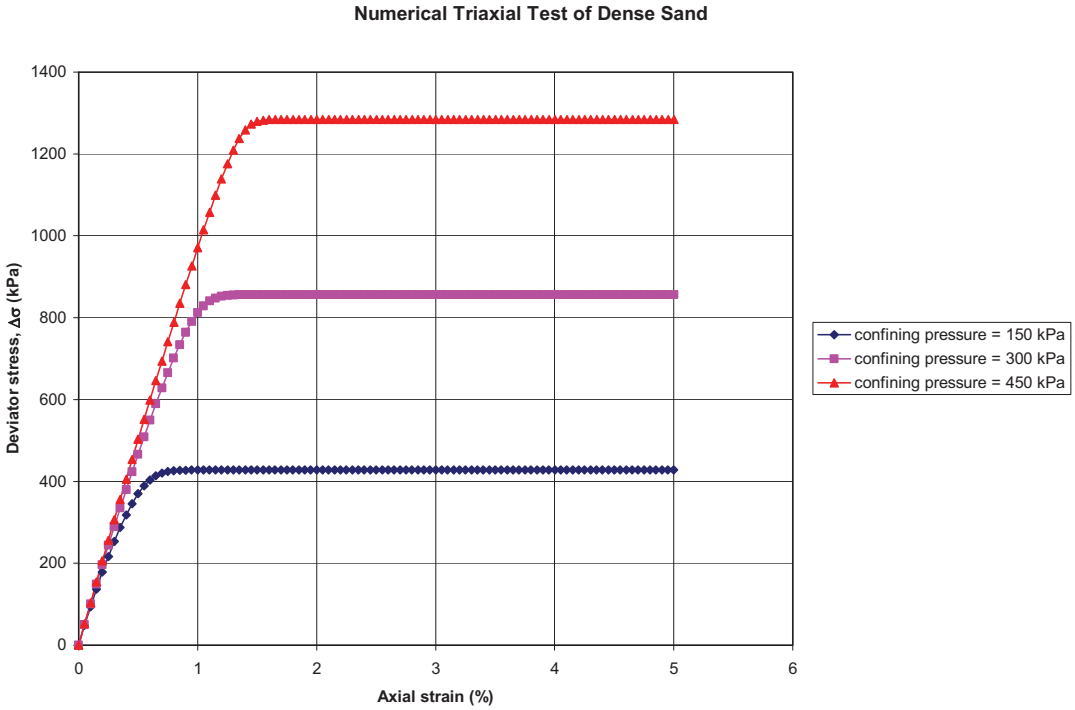

Figure 51. Numerical triaxial compression tests of sand used in the comparative study.

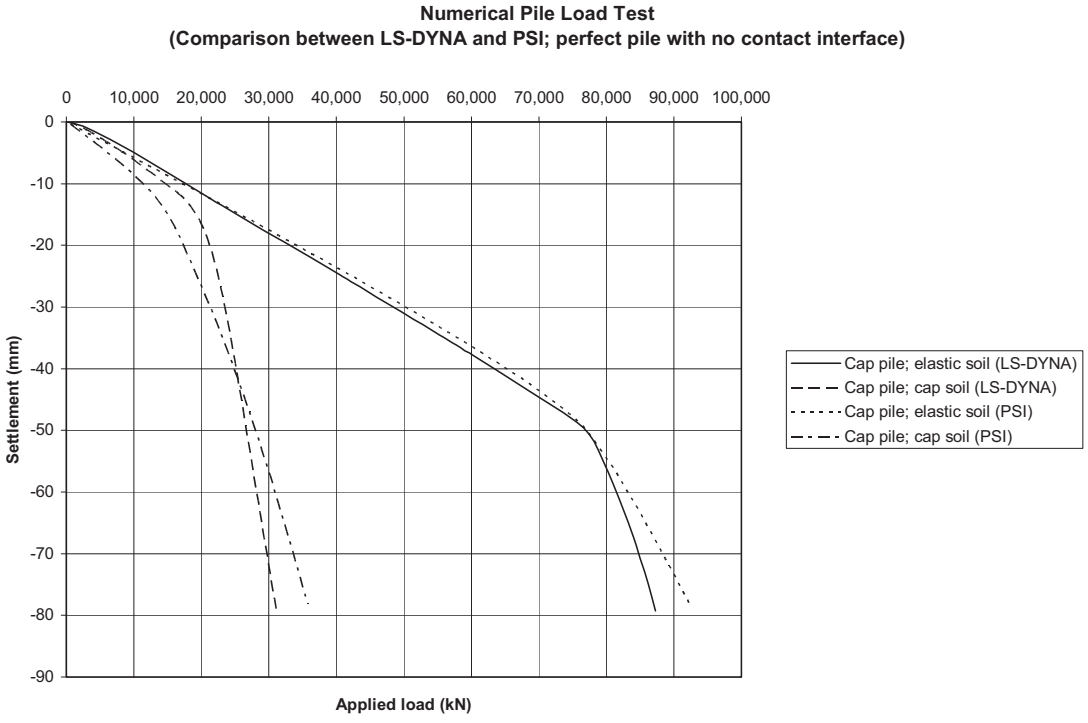

Figure 52. Numerical static shaft-load test comparison between LS-DYNA and PSI with perfect shaft and without contact interface.

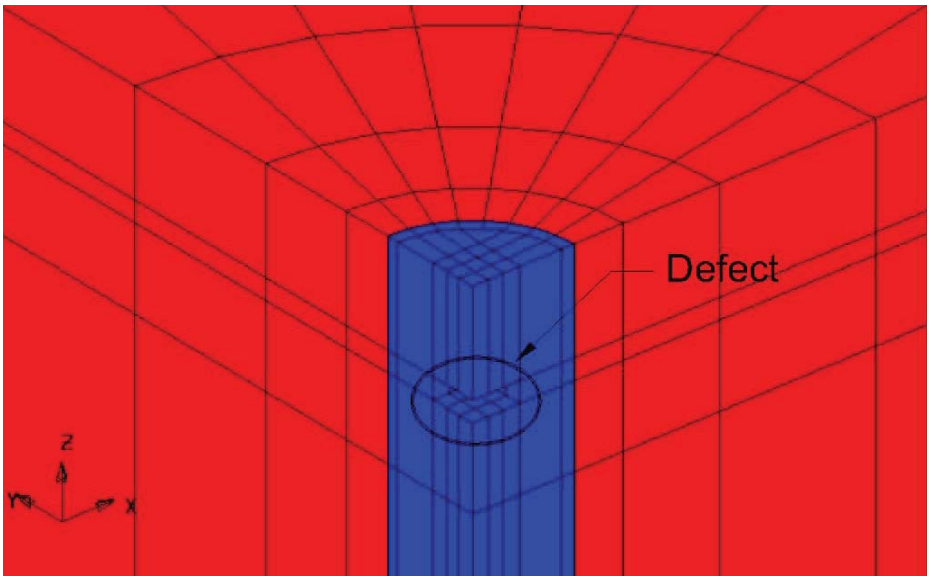

Figure 53. Location of anomaly near the shaft top.

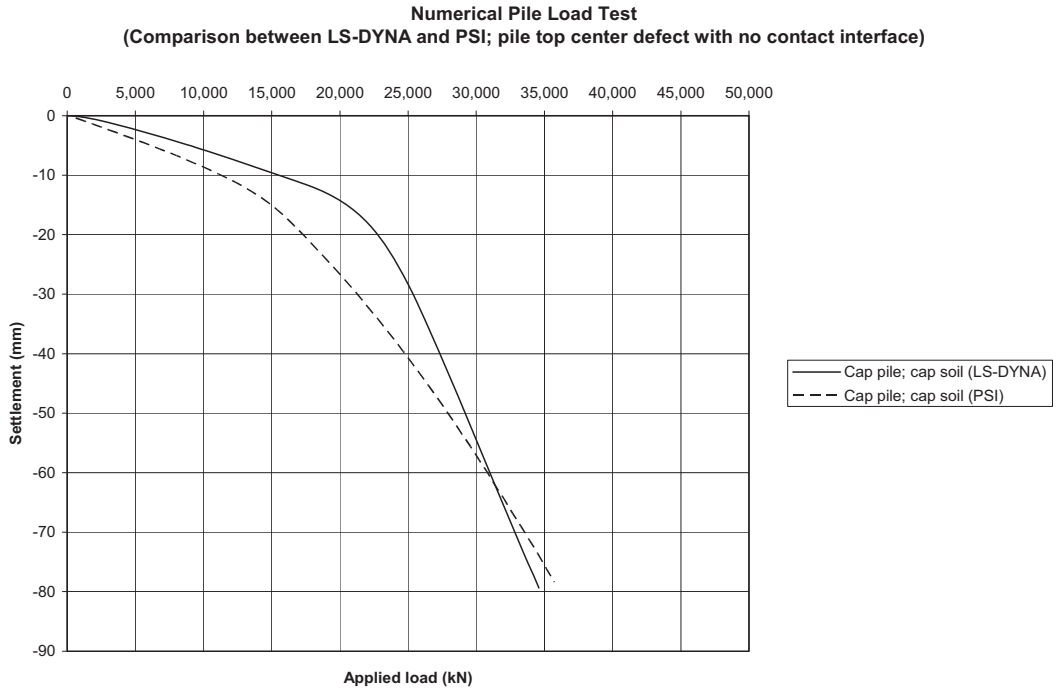

Figure 54. Numerical static shaft-load test comparison between LS-DYNA and PSI with anomaly at top of shaft and without contact interface.

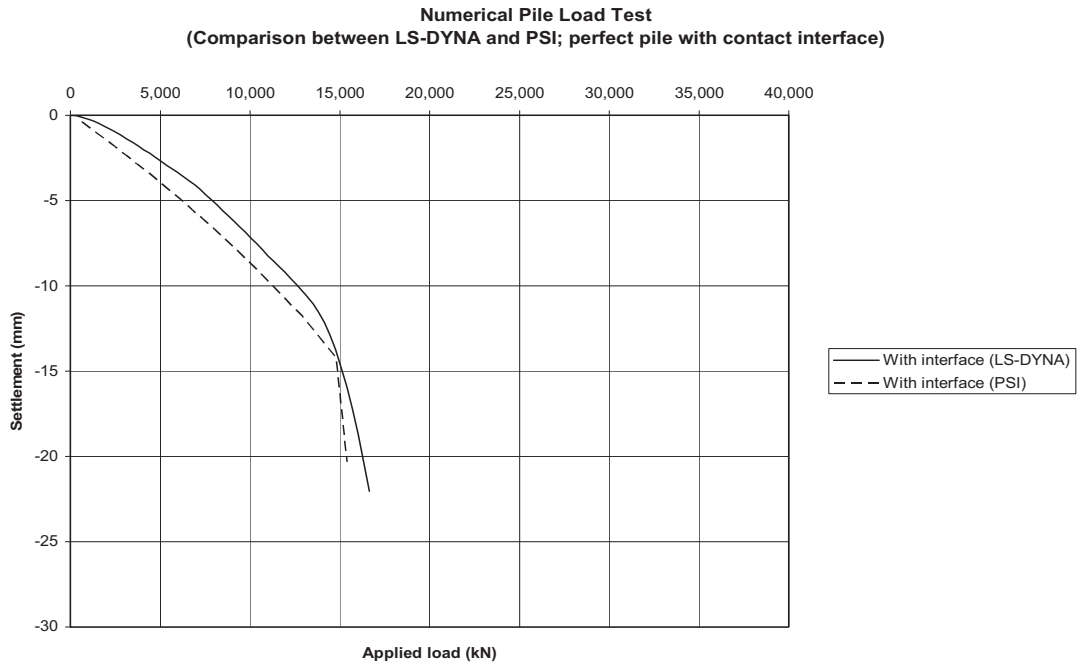

Figure 55. Numerical static shaft-load test comparison between LS-DYNA and PSI with contact interface between shaft and soil.